Exploiting Confinement to Study the Crystallization Pathway of Calcium Sulfate

Clara Anduix-Canto, Mark A. Levenstein, Yi-Yeoun Kim, Jose R. A. Godinho, Alexander N. Kulak, Carlos Gonzalez Nino, Philip J. Withers, Jonathan P. Wright, Nikil Kapur, Hugo K. Christenson, et al.

ADVANCED FUNCTIONAL MATERIALS
www.afm-journal.de

Exploiting Confinement to Study the Crystallization Pathway of Calcium Sulfate

*Clara Anduix-Canto, Mark A. Levenstein, Yi-Yeoun Kim, Jose R. A. Godinho, Alexander N. Kulak, Carlos González Niño, Philip J. Withers, Jonathan P. Wright, Nikil Kapur, Hugo K. Christenson, and Fiona C. Meldrum**

Characterizing the pathways by which crystals form remains a significant challenge, particularly when multiple pathways operate simultaneously. Here, an imaging-based strategy is introduced that exploits confinement effects to track the evolution of a population of crystals in 3D and to characterize crystallization pathways. Focusing on calcium sulfate formation in aqueous solution at room temperature, precipitation is carried out within nanoporous media, which ensures that the crystals are fixed in position and develop slowly. The evolution of their size, shape, and polymorph can then be tracked in situ using synchrotron X-ray computed tomography and diffraction computed tomography without isolating and potentially altering the crystals. The study shows that bassanite ($CaSO_4$ $0.5H_2O$) forms via an amorphous precursor phase and that it exhibits long-term stability in these nanoscale pores. Further, the thermodynamically stable phase gypsum ($CaSO_4$ $2H_2O$) can precipitate by different pathways according to the local physical environment. Insight into crystallization in nanoconfinement is also gained, and the crystals are seen to grow throughout the nanoporous network without causing structural damage. This work therefore offers a novel strategy for studying crystallization pathways and demonstrates the significant impact of confinement on calcium sulfate precipitation, which is relevant to its formation in many real-world environments.

1. Introduction

Understanding the mechanisms by which crystals form promises the ability to control these processes in a vast array of applications. Significant progress has been made thanks to advances in analytical techniques, and it is now recognized that crystallization can occur via processes based on atom-by-atom addition, the assembly of clusters and nanoparticles, and the transformation of liquid-like phases.[1–5] This potentially opens up a huge reaction space, where crystalline materials can form via multiple pathways, which can potentially operate simultaneously.[6] Characterizing crystallization processes therefore becomes highly challenging, where techniques that average over an ensemble of particles,[7] or take a snapshot,[8,9] cannot unambiguously resolve individual pathways. Imaging-based methods that operate in situ and can follow the development of individual crystals to give both morphological and structural data are therefore required.[10,11]

C. Anduix-Canto, M. A. Levenstein,[+] Y.-Y. Kim, A. N. Kulak, F. C. Meldrum
School of Chemistry
University of Leeds
Woodhouse Lane, Leeds LS2 9JT, UK
E-mail: F.Meldrum@leeds.ac.uk

M. A. Levenstein, C. G. Niño, N. Kapur
School of Mechanical Engineering
University of Leeds
Woodhouse Lane, Leeds LS2 9JT, UK

The ORCID identification number(s) for the author(s) of this article can be found under https://doi.org/10.1002/adfm.202107312.

[+]Present address: Université Paris-Saclay, CEA, CNRS, NIMBE, Gif-sur-Yvette 91191, France
[†]Deceased 07-12-2020.

J. R. A. Godinho, P. J. Withers
Henry Royce Institute
Department of Materials
University of Manchester
Manchester M13 9PL, UK

J. P. Wright
European Synchrotron Radiation Facility
BP-220, Grenoble 38043, France

H. K. Christenson[†]
School of Physics and Astronomy
University of Leeds
Woodhouse Lane, Leeds LS2 9JT, UK

DOI: 10.1002/adfm.202107312

Here, we introduce an in situ, imaging-based strategy that exploits confinement effects to study crystallization pathways. Crystallization is conducted within millimeter diameter nanoporous controlled pore glass (CPG) rods such that the developing crystals are fixed in position. In situ synchrotron X-ray micro-computed tomography (μ-CT) and X-ray diffraction computed tomography (XRDCT)[12] can then be used to follow their spatial and structural development in 3D, where the extreme confinement offered by these environments significantly retards crystallization, such that intermediate phases that are short-lived and potentially overlooked in bulk solution are readily observed.[7,13–15] Notably, the CPG rods exhibit uniform, low X-ray absorption, such that images of the developing particles can be recorded with exceptional definition. This system also offers a unique opportunity to study crystallization within porous media, where many important processes including weathering and frost heave,[16–18] the templating of inorganic nanostructures,[19] and biomineralization[20,21] arise from crystallization within porous media such as rocks, polymers or gels.[22]

The potential of this method is demonstrated by its application to the important calcium sulfate system, which is employed in vast quantities in industry,[23] makes a significant contribution to the global sulfur cycle and salt weathering phenomena[24] and whose observation on Mars[25] provides an indicator of past climate conditions. The traditional picture of calcium sulfate mineralogy is that gypsum ($CaSO_4$ $2H_2O$), which is the thermodynamically stable phase at temperatures below 40–60 °C, is the sole phase precipitated from aqueous solutions at room temperature. Bassanite ($CaSO_4$ $0.5H_2O$) becomes the dominant phase above ≈ 95 °C,[23,24] although background electrolytes that reduce the water activity can reduce these transition temperatures such that bassanite has been precipitated at 50 °C with >6 M NaCl.[26] More recent ex situ studies have reported bassanite[27–29] and even an amorphous phase[27,29,30] as intermediates to the aqueous phase precipitation of gypsum at room temperature, although the failure of some in situ synchrotron SAXS/WAXS studies to observe bassanite[31] suggests that sample preparation methods such as the addition of ethanol may alter the crystallization pathway,[24] shedding some doubt on the formation of these phases in aqueous solutions.

Our method enables the crystallization pathway to be characterized in situ and confirms that an amorphous phase forms as a precursor to bassanite. Notably, the short-range structure of this material differs from that of the amorphous precursor to gypsum at 90 °C. This imaging-based approach also provides the first demonstration of long-lived bassanite at room temperature, where the latter is stable for over three weeks in the nanoporous host matrix, and generates information about the crystallization pathway and crystallization within nanoporous media that would be hard to obtain in any other way. By monitoring the evolution of individual particles we show that gypsum can form via multiple, simultaneous pathways in an aqueous solution under ambient conditions and that particles—including gypsum and bassanite—can grow in close proximity without exerting any influence on each other. In combination with ex situ electron microscopy, we can also follow the evolution of the system over multiple length scales and demonstrate that crystals grow throughout the nanoporous network to reach sizes of hundreds of microns without causing any structural damage.

2. Results

2.1. Calcium Sulfate Precipitation within Controlled Pore Glass (CPG) Rods

CPG rods with diameters of 2.8 mm were used to study the precipitation pathways of calcium sulfate. These are ideally suited to in situ experiments, where they comprise a sponge-like, bicontinuous network of ≈7 nm diameter pores with narrow pore size distributions (Figure S1, Supporting Information). The small pore diameter ensures that impurities are excluded from their internal volume such that crystallization occurs within extremely clean environments. They also exhibit uniform low X-ray absorption, which enables exceptional images of particles within the CPG matrix to be recorded, and methods for functionalizing the surfaces of the rods are well-established. Experiments were conducted using unfunctionalized CPG rods, and rods functionalized with carboxyl-terminated monolayers to investigate the influence of the local surface chemistry on the crystallization pathway.

Calcium sulfate was precipitated within CPG rods by inserting a wet rod between two sealed tubes, one containing 3 M $CaCl_2$ and one containing 3 M $(NH_4)_2SO_4$ aqueous solutions (Figure S2, Supporting Information). Counter-diffusion of the calcium and sulfate ions leads to a time-dependent development of supersaturation within the rod, and nucleation occurs once a threshold supersaturation value has been exceeded.[22] The population of particles within the rods then continues to evolve over time. Precipitation within the CPGs was also compared with control experiments performed in bulk solution. In order to maintain the double diffusion configuration, a 1 mm internal diameter glass capillary was substituted for the CPG rod, and the product crystals were analyzed using optical and Raman microscopy. Large aggregates (≈100 μm) of gypsum were observed after 2 min, and no evidence of bassanite was obtained (Figure S3, Supporting Information).

2.2. Simulation of Ion Flow in CPG Rods

The solution conditions under which nucleation occurs within the CPG rods were estimated by modeling the diffusion of ions through the rods using the diffusion equation to determine how the supersaturation profile changed over time (**Figure 1**). This was conducted using the commercial simulation software, COMSOL Multiphysics, where a 2D model was applied and no evaporation was assumed. The rods were considered as perfect cylinders of dimensions 10 × 2.8 mm with porosity of 0.25 and tortuosity of 1.4. Supersaturations were calculated using Visual Minteq, taking into account all ions present. These analyses indicate that the system is supersaturated ($[Ca^{2+}] = [SO_4^{2-}] \approx 60$ mM, $S > 4$) with respect to gypsum[23] at the time at which precipitation is first observed in the CPG. Notably, comparable values have been determined for calcium sulfate precipitation in gel columns.[32] A supersaturation of almost 3 times as high can be estimated after 1.5 h, ($[Ca^{2+}] = [SO_4^{2-}] \approx 180$ mM) when bassanite is first observed by XRD.

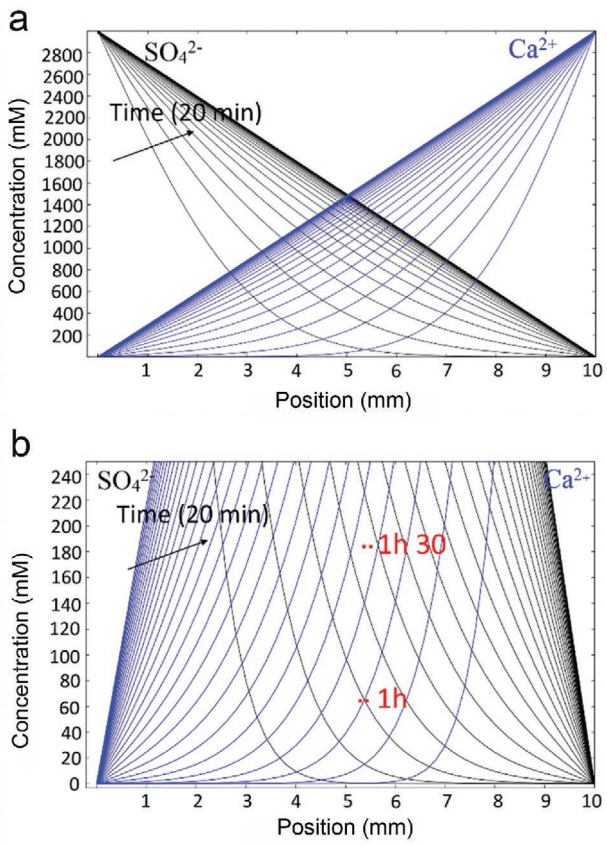

Figure 1. a,b) Predicted ion concentration profiles along the CPG rods as a function of position and the time after injection of 3 M $CaCl_2$ and 3 M $(NH_4)_2SO_4$ solutions. The concentrations of calcium and sulfate ions are represented in blue and black respectively, and the concentration lines are separated by 20 min. 1 h after reagent injection, the ion concentration is ≈ 65 mM at the center of the rod and almost 180 mM after 1 h 30 min. (b) is enlarged to show the concentrations at early times.

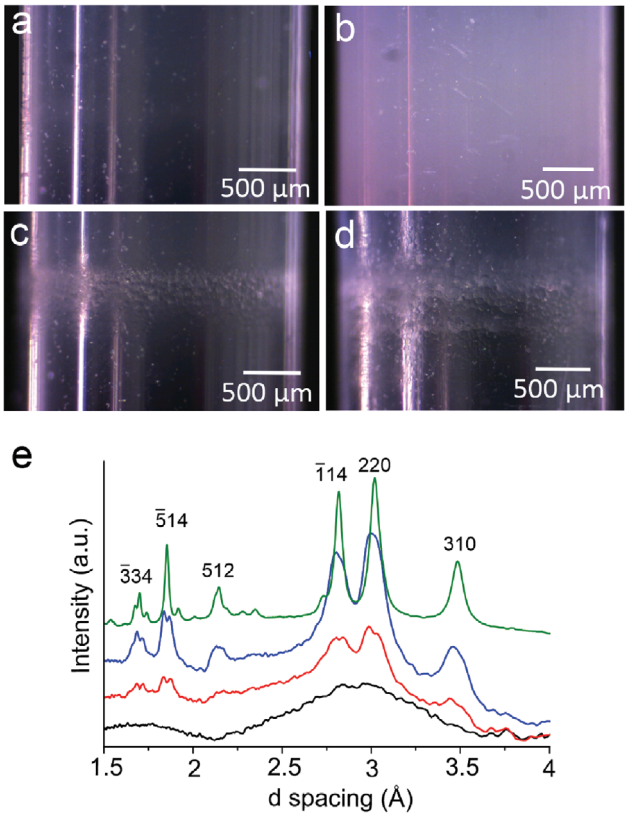

Figure 2. Calcium sulfate precipitation in unfunctionalized CPG rods. a–d) Optical images of the crystallization within the rods after (a) 10 min, (b) 1 h, (c) 2 h, and (d) 4 h. e) XRD patterns of the rod after background subtraction after 1 h (black), 1 h 30 min (red), 2 h (blue), and 7 h (green), showing the peak positions for bassanite.

2.3. In Situ Analysis of Calcium Sulfate Precipitated within Unfunctionalized CPG Rods

Precipitation within the CPG rods was initially evident from the formation of a 2 mm deep, cloudy band in the middle of the rod after 1 h (**Figure 2**a,b). In situ synchrotron X-ray diffraction (XRD) of intact rods using a 0.4 mm beam showed that this material was amorphous (i.e., it exhibited no long-range order), where the diffraction patterns obtained after background subtraction using a CPG rod filled with water exhibited broad bands at ≈ 3 and ≈ 1.7 Å (Figure 2e). The CPG itself scatters to give a broad band at ≈ 4.2 Å (Figure S4, Supporting Information), demonstrating that the bands at 3 Å and 1.7 Å derive from calcium sulfate rather than incomplete background subtraction. The transparency of the rods then started to recover over the next hour, where this was accompanied by the progressive development of a well-defined 0.5 mm deep band in the middle of the rod (Figure 2c). This band became more defined with time, ultimately reaching a thickness of around 1 mm (Figure 2d).

XRD at 1.5 h revealed peaks corresponding to bassanite in addition to the diffuse band from the amorphous material. The signal/noise ratios of the diffractograms obtained at 1 h and 1 h 30 min are comparable, demonstrating that the absence of peaks due to bassanite at 1 h is because the material is amorphous, rather than there being too little bassanite present to obtain an XRD pattern. The amount of bassanite in the rods then continued to increase at the expense of the amorphous phase until sharp peaks were observed after 7h (Figure 2e). Intact rods were also characterized using optical and Raman microscopy, where the laser was focused on large crystals at different positions within the rods (Figure S5, Supporting Information). Peaks at 428 (v_2), 626 (v_3), and 1014 cm^{-1} (v_1) that correspond to bassanite were observed at all times, and no transformation to gypsum was found over the 3-week duration of the experiment. As far as we are aware, the stabilization of bassanite in purely aqueous environments at room temperature for such long periods is unprecedented.

Interestingly, powder XRD analysis of amorphous calcium sulfate produced in bulk solution at 90 °C yielded diffractograms comprising two diffuse maxima at approximately d = 4.2 Å and d = 8.8 Å.[33] This amorphous phase transformed to gypsum alone, without any bassanite as an intermediate phase. In our experiments, in contrast, the amorphous precursor phase principally transformed to bassanite. This suggests—as has been demonstrated for calcium carbonate[34]—that "amorphous calcium sulfate" may not constitute a single material, but may vary in composition and structure according to the conditions under which it is precipitated.

2.4. Origin of the Extended Stability of Bassanite

Both confinement effects—which invariably extend the lifetimes of metastable phases[7]—and the presence of high background concentrations of ammonium chloride in the system are expected to contribute to the extended lifetime of the bassanite within the CPGs. Although bassanite is not usually precipitated in aqueous solutions below temperatures of ≈ 95 °C, this is reduced in the presence of high salt concentrations,[23] where a value of 80 °C was reported for 4.3 M NaCl[35] and 50 °C at >6 M NaCl.[26] High concentrations of ammonium chloride also increase the solubility of gypsum[36,37] and are thus expected to have a similar effect.

Experiments were therefore conducted to estimate the relative importance of confinement effects and high ammonium chloride concentrations on the stability of bassanite in the CPGs. Bassanite was precipitated at 80 °C in bulk solutions by combining equal volumes of 3 M aqueous solutions of $CaCl_2$ and $(NH_4)_2SO_4$, and by combining equal volumes of 300 mM $CaCl_2$ and $(NH_4)_2SO_4$ solutions, where the latter were prepared by dissolving the solids in 5 M $(NH_4)_2Cl$ aqueous solutions. The suspensions of bassanite were then cooled to room temperature over 10 min. In both cases, transformation to gypsum occurred within 10 min (Figure S6, Supporting Information). As a final demonstration, the experiments were repeated within the CPG rods with 250 mM reagents. Bassanite was now detected after 7 h as compared with 1 h 30 min for the 3 M reagents and was again stable for over 3 weeks in these environments (Figure S7, Supporting Information). Gypsum alone was observed in control experiments with glass capillaries at these concentrations. This conclusively demonstrates that the high stability of bassanite within the CPGs therefore principally derives from confinement effects, as seen in many other systems.[7,13,14]

2.5. In Situ Tomography of Calcium Sulfate Precipitation within Unfunctionalized CPGs

The development of particles within the CPG rods was observed in situ using μ-CT and XRDCT, where these reveal how the population of individual particles develops in 3D over time (**Figure 3**). μ-CT generates high-quality images of the particles based on the absorption of the X-ray beam, while XRDCT is able to 3D image and identify the crystal polymorph of the individual crystal grains (although at somewhat lower spatial and time resolution) non-destructively over time. Experiments were conducted by inserting the ends of CPG rods into plastic tubes, sealing the $CaCl_2$ reservoir, and mounting the system vertically on the rotating stage with the $(NH_4)_2SO_4$ reservoir at the top. Alternating diffraction and imaging scans were recorded over time. XRDCT was performed by recording 2D XRD patterns at different z heights along the CPG rods, and these data were used to generate spatial diffraction maps of individual cross-sectional slices. 2D XRD patterns were also recorded of large volumes of individual samples using a 0.4 × 0.4 mm^2 beam at 40 keV and exposure times of 1 s. This yielded average data of the crystal phases present within a 0.16 mm^2 area at the center of the rod. The crystals within the rods were imaged using attenuation μ-CT, where 3D tomograms were computationally reconstructed from the projection images.

μ-CT images recorded after 3h showed that the visible band in the middle of the rod comprised spheroidal crystals that were tens, to several hundreds of microns in size, and that the number density of crystals over 50 μm in size was 20 to 40 crystals mm^{-3} (Figure 3a,b). The number and sizes of the crystals continued to increase with time, at growth rates of approximately 36 $\mu m^3\ h^{-1}$, and after 24 h formed a

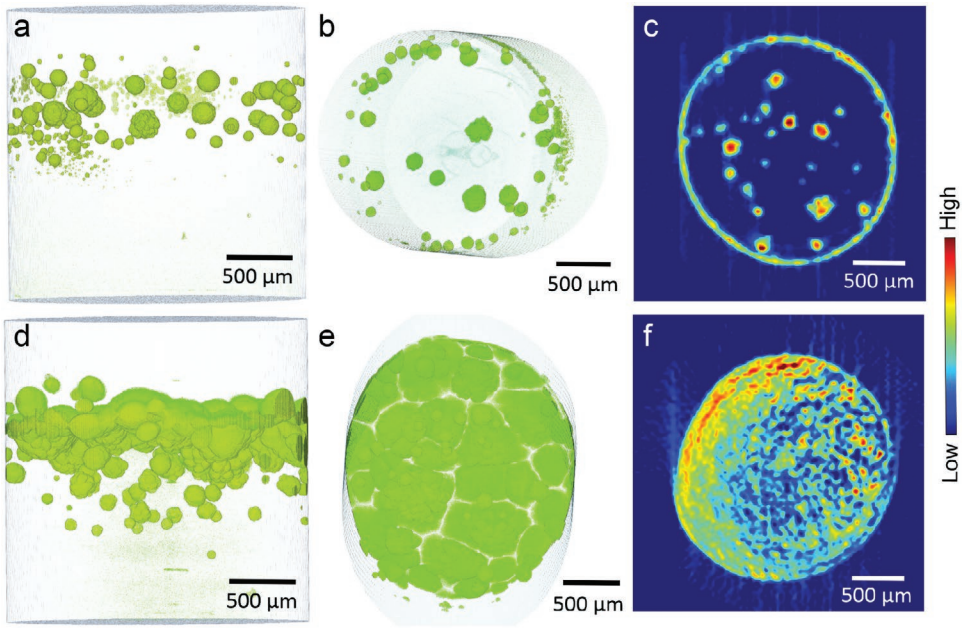

Figure 3. CT imaging of calcium sulfate precipitation in an unfunctionalized CPG rod. a,b,d,e) 3D rendering from the μ-CT showing bassanite crystals precipitated in a rod after (a,b) 3h and (d,e) 24 h, where the tomograms shown in (a) and (d) are parallel to the long axis of the rod and (b) and (e) are perpendicular. c,f) 2D spatial diffraction maps of bassanite crystals in the rod after (c) 7 and (f) 24 h, based on the (110) reflection from bassanite. Low and high intensities are shown in blue and red respectively.

continuous band that blocked the rod (Figure 3d,e). The structures of the calcium sulfate crystals were investigated using XRDCT, where this was performed over the middle of a rod at 7 and 24 h. The diffraction maps showed that the crystals precipitated at 7 h were located throughout the rods and bassanite was the only phase detected (Figure 3c). The large mass of crystals present after 24 h was also identified as bassanite using XRDCT (Figure 3f and Figure S4, Supporting Information).

2.6. Influence of Crystal Growth on the CPG Matrix

While μ-CT reveals how a population of spherical bassanite particles—that reach sizes of hundreds of microns—develop within the rods, it is emphasized that the CPG matrix presents a sponge-like network of pores that are just 7 nm in diameter. It is therefore intriguing to consider how the crystals grow within this network. As the rods are relatively fragile, it could also be envisaged that crystallization could cause significant damage to the matrix, resulting in the crystals being located within a cavity in the porous glass. Electron microscopy was therefore used to examine the nanoscale structure of the CPG containing the crystals.

Scanning electron microscopy (SEM) of a cross-section through the rods revealed the presence of spheroidal domains corresponding to the crystals (**Figure 4**a,4b), where energy dispersive X-ray (EDX) maps confirmed that these were rich in Ca and S (Figure S8, Supporting Information). These images demonstrate the integrity of the porous glass matrix on the micron scale. Transmission electron microscopy (TEM) examination of lamellae prepared from areas of the rods containing crystals using focused ion beam (FIB) milling then enabled these structures to be characterized at the nanoscale. Bright-field TEM images (Figure 4c) and STEM-EDX (scanning TEM and EDX analysis) elemental mapping (Figure 4d) showed that the crystals grew uniformly throughout the interconnected pores, and confirmed that the micron-sized crystals formed without damage to the CPG. Selected area electron diffraction (SAED) also confirmed that the crystals were polycrystalline bassanite (Figure 4e) and showed that they exhibited preferential orientation that is characteristic of spherulitic crystals. High-resolution imaging also revealed single-crystal domains corresponding to bassanite (Figure 4f).

2.7. Calcium Sulfate Precipitation within Carboxylate-Functionalized CPGs

The role of the CPG surface chemistry in directing crystal growth was investigated by precipitating calcium sulfate within CPG rods whose surfaces had been functionalized with carboxyl-terminated monolayers. Little difference was seen in the rate of crystallization as compared with unfunctionalized rods, but in stark contrast to the latter system when bassanite alone was observed over 3 weeks, both bassanite and gypsum were observed after 1 h 15 min when the estimated concentrations were $[Ca^{2+}] = [SO_4^{2-}] \approx 150–180$ mM (Figure S9, Supporting Information). Remarkably, the images are of such high quality that these phases could be readily distinguished in the in situ

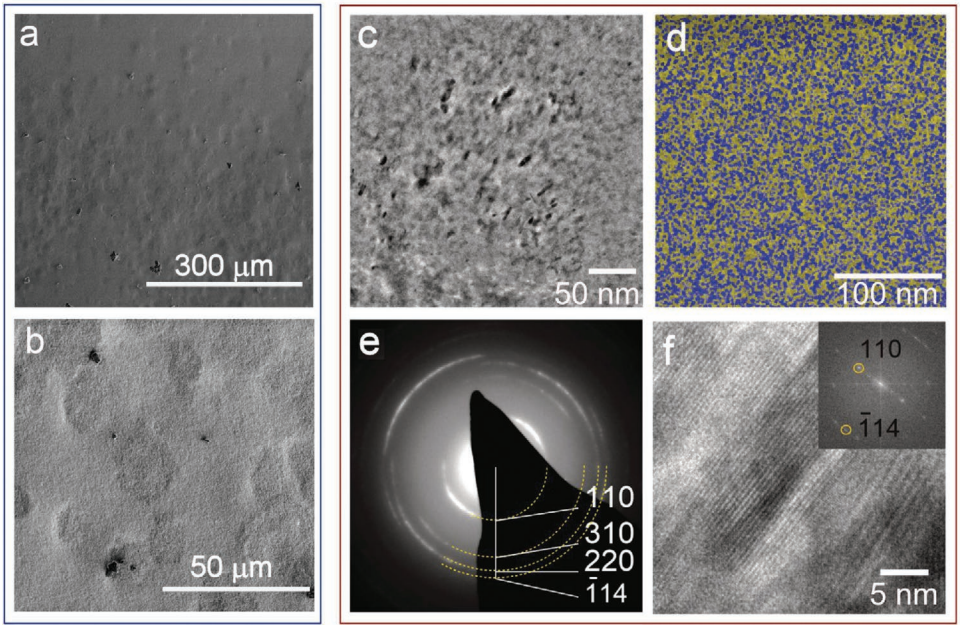

Figure 4. SEM, TEM, and STEM Analysis of calcium sulfate precipitates in unfunctionalized CPG rods. a,b) SEM images of a cross-section through a CPG rod 7 h after the outset of the experiment. c–f) Images of a thin section through a rod after 5 h reaction time. (c) Bright-field TEM image showing that the crystals grow without damaging the porous network. (d) HAADF-STEM elemental mapping of the same thin section, where Ca (from $CaSO_4$) is represented in blue and Si (from the CPG) is shown in yellow. (e) SAED pattern using 500 nm aperture which confirms that the crystals are bassanite. (f) A high-resolution TEM image and FFT (inset) showing the bassanite crystal lattice with 6 Å and 2.8 Å spacings which correspond to the {110} and {114} planes respectively. This single-crystal region is part of the micron-scale polycrystalline particle.

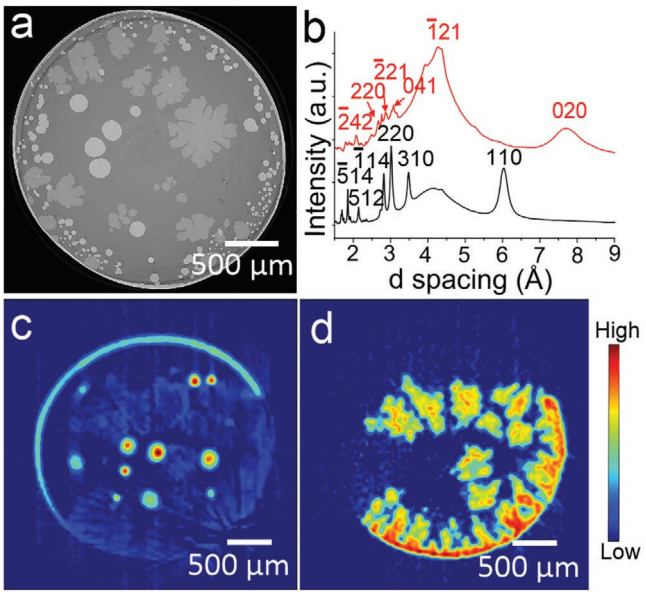

Figure 5. Calcium sulfate precipitation in a carboxylate-functionalized CPG rod. a) A 2D µ-CT slice of calcium sulfate crystals precipitated after 2 h 30 min, where the brighter circular crystals are bassanite and the darker, dendritic crystals are gypsum. b) Analysis of a sample by diffraction, where the black curve corresponds to bassanite and the red to gypsum. c,d) The assignment of the phases of individual particles is made using diffraction tomography, where c) is plotted using the (110) reflection from bassanite and d) the (020) reflection from gypsum. Different samples are shown for (a) and (b–d), where the amount and distribution of the mineral deposits vary from slice to slice.

μ-CT images, where the denser bassanite crystals exhibit higher attenuation contrast than gypsum crystals (**Figure 5**A). The morphologies of the bassanite and gypsum crystals were also entirely distinct, where bassanite was spheroidal and gypsum dendritic. The assignment of both phases was confirmed by in situ XRD (Figure 5b) and XRDCT (Figure 5c,d and Figure S10, Supporting Information), where the resolution was sufficient to identify the distinct spherical and dendritic morphologies and therefore conclusively assign the polymorph.

The evolution of the calcium sulfate crystals in the carboxylate-functionalized CPGs was also studied over time. Typically, a higher number density of particles initially forms around the exterior of the rods (**Figure 6**a), where this can be attributed to slow evaporation from the rods and thus a local increase in supersaturation. More bassanite than gypsum particles are present at early times (Figure 6a and Figure S10, Supporting Information), but both phases continue to nucleate and grow until the rod becomes blocked. Notably, the gypsum particles grew significantly faster than the bassanite (Figure 6b)—as is consistent with a spherulitic growth mechanism—such that the total volume of the gypsum in the CPG ultimately exceeds that of bassanite.

2.8. Coexistence of Bassanite and Gypsum within CPG Rods

That both bassanite and gypsum formed within the functionalized CPG rods also provided a unique opportunity to study the influence of adjacent crystals—and in particular those of different phases—on each other. The images show that gypsum crystals either form de novo in the glass matrix (red arrows) or are very close to existing bassanite crystals (Figure 6g,h, black arrows). While the resolution of the µ-CT images was not sufficient to conclusively determine whether gypsum nucleates directly on bassanite particles (we cannot observe the nanopores), the 3D tomographic images confirm the close proximity of these particles. Interestingly, in neither case did the growing gypsum crystals induce dissolution or transformation of bassanite crystals in their vicinity.

This can be attributed to the interconnectivity of the pores and the continuous replenishment of ions from the reservoirs. If crystal growth is kinetics-limited rather than diffusion-limited, then sufficient ion transport to a gypsum crystal occurs to ensure that it grows without developing a depletion zone that would induce dissolution of the neighboring bassanite. Long-term incubation of the rods would ultimately be expected to give rise to the growth of the gypsum crystals at the expense of the bassanite.

2.9. Transformation of Bassanite to Gypsum within CPG Rods

Our ability to distinguish between gypsum and bassanite in the µ-CT images also allowed us to investigate the mechanism of transformation of bassanite to gypsum. Here, transformation was induced by exchanging the reagent solutions for water after 2 h reaction time. In situ µ-CT revealed a direct transformation of bassanite to the more hydrated gypsum after a further 5–8 h (**Figure 7** and Figure S11, Supporting Information), where this occurs from the outer surface towards the center, as can be seen from the distinct contrast of the two phases in the µ-CT images in the 2D cross-sections (Figure 7a,b). Notably, the morphology of the original bassanite is retained, such that the product gypsum crystals exhibit a spherical morphology rather than the characteristic dendritic form that occurs on direct precipitation. This is also seen in the 3D µ-CT rendering of the crystals after transformation (Figure 7c,d).

Given that gypsum has a larger molar volume than bassanite, it might be expected that transformation of bassanite to gypsum could lead to structural damage of the CPG. However, no evidence of any cracks or structural inhomogeneities on the micron scale was obtained from the µ-CT images. Analysis at the nanoscale was carried out by isolating the CPG rod during transformation and preparing a thin section for cryo-TEM analysis using FIB. Imaging of these sections again demonstrated the integrity of the CPG matrix (Figure S12, Supporting Information). It is noted that although Raman microscopy confirmed that gypsum was present in these samples, no gypsum could be identified by electron diffraction. It has been previously reported that FIB sample preparation damages gypsum, rendering crystals unstable under subsequent TEM analysis.[38]

That no damage was observed suggests that even in the CPGs the transformation of bassanite to gypsum occurs via a dissolution/ reprecipitation mechanism, as has been observed in bulk solution[39] and in humid environments.[40] As the transformation is pseudomorphic, and proceeds from the outer

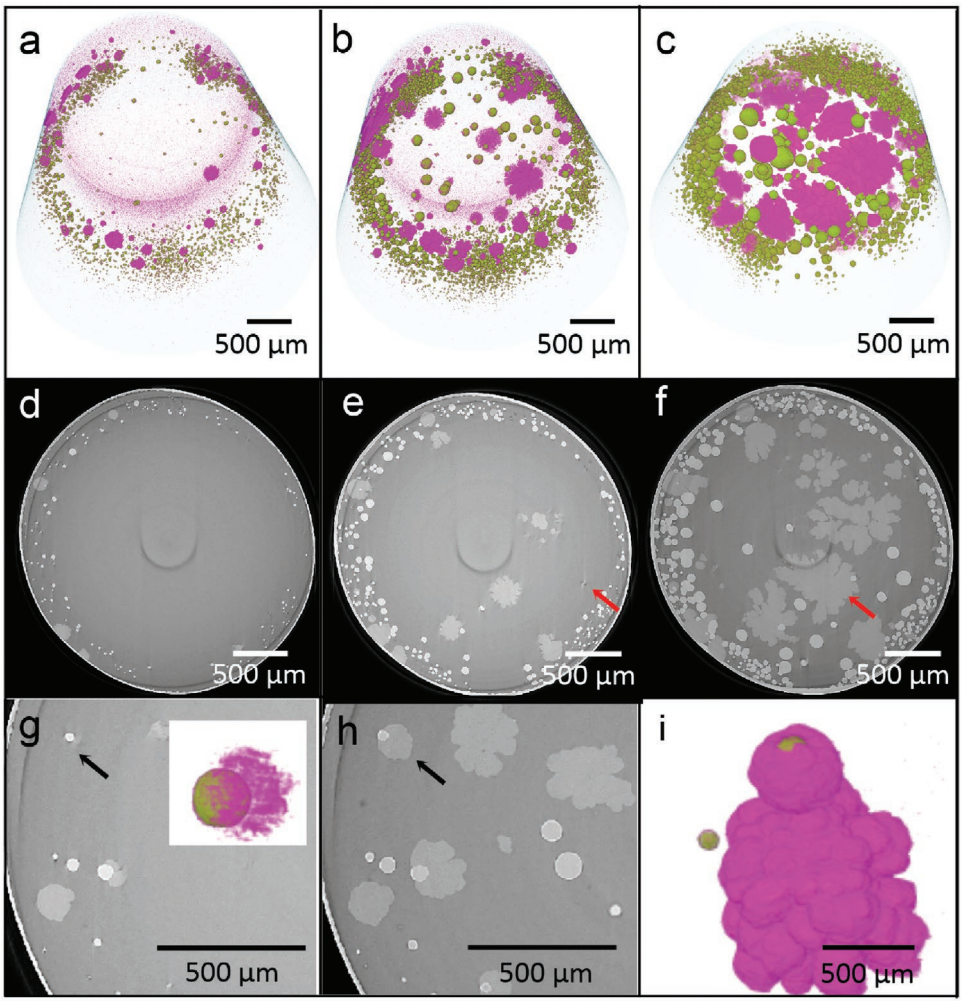

Figure 6. Evolution of calcium sulfate crystals in carboxyl-functionalized CPG rods. a–c) 3D μ-CT rendering of bassanite (green) and gypsum (pink) inside the rod (rendered semi-transparent) after (a) 1 h 45 min, (b) 2 h, and (c) 2 h 30 min from solution injection. d–f) 2D sections within the precipitation band, where bassanite is the light grey and gypsum is darker grey after (d) 1 h 45 min, (e) 2 h, and (f) 2 h 30 min. Gypsum was frequently observed to form in the absence of any bassanite precursor (red arrows). Gypsum growing from or very close to bassanite crystals (black arrow) is also observed in the 2D cross-sections and 3D colorized volume renderings after g) 2 h and h,i) 2 h 30 min.

surface, inwards, this indicates that dissolution/reprecipitation must occur at a local level, where this may be facilitated by water lying between the crystal and the CPG surface.[41,42]

3. Discussion

The imaging-based approach described here offers a unique means of studying crystallization mechanisms. Many of the techniques that are used to study crystallization processes such as IR, Raman, powder XRD, and SAXS sample and average an ensemble of particles, and thus cannot easily distinguish between individual pathways. Therefore, minor or short-lived pathways are masked by dominant ones. It is also difficult to determine whether phases transform via solid-state transformations or dissolution/ precipitation processes. These problems can be overcome using imaging-based techniques to follow the evolution of the morphologies and structures of a population of individual particles. Of these, µ-CT is both widely available and well-suited to in situ analyses. It can also sample large volumes, and by conducting measurements in situ, artifacts arising from sample preparation are eliminated. µ-CT has been previously employed to image the precipitation of salts within porous rocks[43–45] and between glass beads,[46,47] in relation to weathering processes. However, our data demonstrate that when applied to crystallization within nanoporous CPG rods, images of exceptional definition are obtained, where we were even able to distinguish between polymorphs based on their differing absorption contrast.

Calcium sulfate crystallizes extremely slowly within the nanoporous CPGs, allowing us to observe the possible pathways by which this occurs. Indeed, in bulk solution, intermediate phases are often too short-lived, or are present as too small a fraction to enable their identification and characterization. The first phase formed is amorphous, where this is confirmed with in situ analysis, without the addition of solvents that may induce its precipitation. Large quantities of bassanite are then generated, which are stable for the entire duration of the

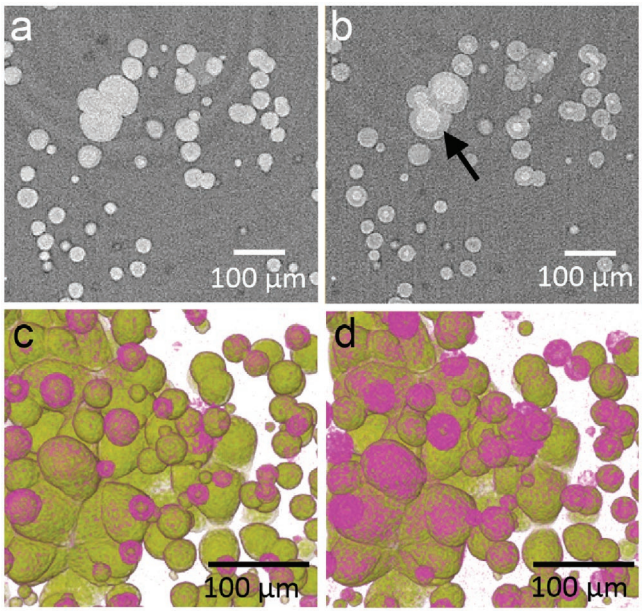

Figure 7. Transformation of bassanite to gypsum in a carboxylate-functionalized CPG rod. a,b) 2D CT cross-sections and c,d) 3D µ-CT renderings of bassanite (green) to gypsum (pink) transformation over time 5 h (a,c) and 8 h (b,d) after the 3 M reagents are replaced by H_2O. The bassanite crystals can be seen to transform to gypsum with retention of morphology, as shown by the dark halo surrounding a bright core (arrowed). This is also seen in (c,d) where bassanite is represented with green and gypsum with pink.

experiments (over three weeks). As far as we are aware, this is the first in situ demonstration of bassanite precipitation at room temperature in a purely aqueous solution.

Perhaps the most exciting outcome of our technique, however, is that it enables us to show that simultaneous, independent crystallization pathways can operate. While bassanite alone formed in the unfunctionalized rods over the duration of the experiment, both bassanite and gypsum formed in the carboxylate-functionalized CPG rods. The gypsum particles were not the product of a direct transformation from bassanite, and formed at the same time as new bassanite particles were forming within the rods. It would be impossible to observe these two mechanisms using bulk measurements, where the data could simply be interpreted as bassanite converting to gypsum.

That a common amorphous phase can transform into different calcium sulfate minerals is consistent with the nucleation pathway suggested by in situ SAXS/WAXS studies of calcium sulfate formation in bulk solution. Primary clusters initially form through the assembly of Ca^{2+} and SO_4^{2-} ions,[26,31,48] and then assemble into loose domains. These then collapse to form amorphous aggregates which crystallize on the reorganization of the constituent primary species.[26,31] It has therefore been proposed that gypsum, bassanite, or anhydrite can form from a common amorphous precursor phase, depending on the reaction conditions.[24,31,38] However, as these studies only observed a transformation to gypsum at room temperature,[31,48] or to bassanite when the reaction was conducted at 90 °C in 4.3 M NaCl,[26] this could not be proven. Our study therefore provides the first direct experimental evidence to support this hypothesis, where the amorphous precursor phase can transform to both gypsum and bassanite under control of the local reaction environment.

Considering then the environment provided by the CPG, confinement can exert many effects on crystal nucleation and growth, where these are dependent on factors including the length-scale, geometry, and material composition of the confinement system.[7,13,49] Metastable polymorphs frequently exhibit very long lifetimes within small volumes,[13,14,29,50] and confinement can even change the crystallization pathway.[51] Huge reductions in nucleation rates are also commonly observed,[52,53] which can arise from a range of phenomena. The most general is the exclusion of impurities, where this has been demonstrated in studies of nucleation in small droplets, many of which will be impurity-free.[54,55] The CPGs have a large, continuous volume but will exclude impurities due to the very small diameters of the pores. Their internal surfaces are also expected to be free of topographical features such as scratches and pits[49] that can promote nucleation on macroscopic substrates.[56,57]

That the amorphous phase is relatively long-lived in the CPG can therefore be attributed to the fact that heterogeneous nucleation is suppressed in these environments. Conversely, amorphous calcium sulfate is either very short-lived in bulk aqueous solutions,[27] or cannot be observed at all. Given that the surface energy is a critical component of the nucleation rate, the energy barrier to the formation of the amorphous phase would be expected to be lower than that of bassanite (γ= 9 mJ m^{-2}),[58] and significantly lower than that of gypsum (γ= 41 mJ m^{-2}).[59] The suppression of heterogeneous nucleation would therefore be expected to have the greatest impact on the nucleation of gypsum, giving the opportunity for the amorphous phase and bassanite to form.

The crystallization pathway in our system is also governed by the surface chemistry of the nanoporous CPG, which may derive from factors including differences in the distribution of ions in nanopores as compared with adjacent to a planar surface,[60] and in the structure and dynamics of the water in the nanopores as compared with bulk solution.[61] Indeed, computer simulations have predicted up to 3 monolayers of surface water (≈0.9 nm) in silica nanopores[62] and experiments have shown that water in nanopores exhibits an anomalously low dielectric constant.[61] Water also plays a key role in directing the crystallization pathway of calcium sulfate system, where pure bassanite can be precipitated from water/ solvent mixtures at moderate temperatures,[63–65] with the most polar solvents being the most effective. High salt concentrations also promote bassanite, although there are no previous reports of this occurring at room temperature.[23,26,35] The different water structure and charge distribution in the nanopores in uncoated and carboxylate-functionalized CPG are therefore expected to influence the structural rearrangement of the amorphous phase, leading to the formation of either bassanite or gypsum. Although the carboxylate-functionalized pores are weakly charged in the pH regime of our experiments (5.5–6),[66] the strong chemical interactions that occur between the calcium ions and the carboxylate groups are expected to lead to a concentration of calcium ions at the monolayer surface.

4. Conclusions

In summary, we have described an imaging-based strategy that exploits confinement effects to track the evolution of a population of individual particles in situ using synchrotron X-ray computed tomography and diffraction computed tomography, and therefore explore the possible pathways by which crystals form. Application to the calcium sulfate system revealed that concurrent pathways can operate in an aqueous solution, and that the amorphous precursor phase can transform into either bassanite or gypsum according to the local environment. This is consistent with developing ideas about crystallization mechanisms, where the simultaneous operation of distinct pathways involving intermediary, metastable phases may prove to be the rule rather than the exception. Our work also gives new insight into crystallization within nano-scale environments, where we show that crystals grow through the nanoporous network without causing structural damage and that the transformation of bassanite to gypsum in these confined volumes occurs via a pseudomorphic transformation. The crystallization pathway is directed by the surface chemistry of the rod, which suggests that the structure and dynamics of the water within the nanopores may play a role in polymorph selection. It is envisaged that our experimental approach can be used to study processes such as weathering and biomineralization, which will ultimately enable us to predict and control crystallization within porous media. We also expect that the continued development of techniques such as X-ray ptychography[67,68] will offer in situ measurements at enhanced spatial resolution, thereby permitting the observation of earlier stages of crystallization.

5. Experimental Section

Crystallization in Controlled Pore Glass (CPG) Rods: The CPG rods used had dimensions of 2.8 mm in diameter, were 10 mm in length, and possessed a narrow pore size distribution with mean pore size ≈7 nm, surface area of 120 ± 10 m^2 g^{-1}, and porosity of 25 ± 4%. The CPG rods were first filled with Milli-Q DI water by immersing them in water for at least 4h. Calcium sulfate was then precipitated within the rods by inserting their ends into pieces of plastic tubing, which were in turn inserted into glass tubes. 3 M $CaCl_2$ and $(NH_4)_2SO_4$ solutions were injected into these glass tubes, which were sealed.

In Situ Synchrotron X-Ray Diffraction (XRD), Micro-Computed Tomography (μ-CT), and Diffraction Computed Tomography (XRDCT): Combined synchrotron μ-CT and XRDCT[12,69] were used to observe the formation of the different calcium sulfate phases. Experiments were conducted at ID11 (Materials Science beamline) at the European Synchrotron Radiation Facility (ESRF) Grenoble, France. CPG rods were inserted into glass tubes and the seal closing the $CaCl_2$ reservoir was glued to an M4 screw attached to a rotating stage. The system was mounted vertically on the rotating stage with the $(NH_4)_2SO_4$ reservoir at the top. Alternate diffraction and imaging scans were recorded.

XRDCT was performed by recording 2D XRD patterns at different z heights along the CPG rods, and these data were used to generate spatial diffraction maps of individual cross-sectional slices. XRDCT data were collected at 86 positions across the width of the 2.8 mm CPG rods with a 50 × 50 μm^2 beam unless otherwise stated. 2D XRD patterns were also recorded of large volumes of individual samples using a 0.4 × 0.4 mm^2 beam and exposure times of 1 s. This yielded average data of the crystal phases present within a 0.16 mm^2 area at the center of the rod. A diffraction pattern of a rod filled with water was used to subtract the glass background from the diffraction patterns of the CPG/calcium sulfate samples. The crystals within the 2.8 mm CPG rods were also imaged using μ-CT at beamline I13-2 at Diamond Light Source, where 3D tomograms were computationally reconstructed from the projection images. The images were collected with a high-resolution camera with a 2560 × 2160 pixel array and an effective pixel size of 1.6 μm.

Additional Characterization Methods: The surface areas, pore sizes, and porosities of the CPG rods were determined using Barrett–Joyner–Halenda (BJH) and Brunauer–Emmett–Teller (BET) surface area analysis with nitrogen gas. Raman spectra of crystals growing inside the CPG rods were collected in situ from intact rods. The laser was focused on different positions within the rod, where crystals were observed. TEM and Scanning Transmission Electron Microscopy (STEM) were used to image cross-sections of CPG rods. Cross-sections were prepared using FIB milling.

Supporting Information

Supporting Information is available from the Wiley Online Library or from the author.

Acknowledgements

The authors are grateful to Patrick Huber, (Technische Universität Hamburg) for advice on sourcing the CPG rods and Charles Landry for advice and help with manufacturing these. The authors would like to thank Diamond Light Source for beamtime (MT13578 and MT17314) on beamline I13-2 and the staff of beamline I13 for their assistance with data collection and processing, especially Dr. Kaz Wanelik and Dr. Andrew Bodey. This work was supported by a Leverhulme Trust award (F.C.M and Y.Y.K) and Engineering and Physical Sciences Research Council (EPSRC) Platform Grant (F.C.M. and H.K.C., EP/N002423/1), and an EPSRC Programme Grant which funds the Crystallization in the Real World Consortium (EP/R018820/1, F.C.M. and Y.Y.K.). J.R.A.G. was supported by an EPSRC Platform grant (EP/M010619/1) and P.J.W. is grateful to the ERC for advanced grant funding through CORREL-CT Grant No. 695638. The authors thank the ESRF for granting beamtime at ID11 (proposals CH4778 and CH5141) and Dr. Carlotta Giacobbe for her help during and after the beamtime. This article is dedicated to Hugo, who is much missed.

Conflict of Interest

The authors declare no conflict of interest.

Data Availability Statement

The data that support the findings of this study are openly available in the Research Data Leeds Repository at https://doi.org/10.5518/1041.[70]

Keywords

amorphous calcium sulfate, bassanite, confinement, crystallization, gypsum, X-ray tomography

Received: July 27, 2021
Published online: September 14, 2021

[1] D. Gebauer, P. Raiteri, J. D. Gale, H. Colfen, *Am. J. Sci.* **2018**, *318*, 969.
[2] D. Gebauer, M. Kellermeier, J. D. Gale, L. Bergstrom, H. Coelfen, *Chem. Soc. Rev.* **2014**, *43*, 2348.
[3] P. R. ten Wolde, D. Frenkel, *Science* **1997**, *277*, 1975.

[4] P. G. Vekilov, *Nanoscale* **2010**, *2*, 2346.
[5] J. J. De Yoreo, P. U. P. A. Gilbert, N. A. J. M. Sommerdijk, R. L. Penn, S. Whitelam, D. Joester, H. Zhang, J. D. Rimer, A. Navrotsky, J. F. Banfield, A. F. Wallace, F. M. Michel, F. C. Meldrum, H. Coelfen, P. M. Dove, *Science* **2015**, *349*, aaa6760.
[6] M. H. Nielsen, S. Aloni, J. J. De Yoreo, *Science* **2014**, *345*, 1158.
[7] F. C. Meldrum, C. O'Shaughnessy, *Adv. Mater.* **2020**, *32*, 2001068.
[8] W. Habraken, J. H. Tao, L. J. Brylka, H. Friedrich, L. Bertinetti, A. S. Schenk, A. Verch, V. Dmitrovic, P. H. H. Bomans, P. M. Frederik, J. Laven, P. van der Schoot, B. Aichmayer, G. de With, J. J. DeYoreo, N. Sommerdijk, *Nat. Commun.* **2013**, *4*, 1507.
[9] L. Houben, H. Weissman, W. S. G. , B. Rybtchinski, *Nature* **2020**, *579*, 540.
[10] Z. H. Ou, Z. W. Wang, B. B. Luo, E. Luijten, Q. Chen, *Nat. Mater.* **2020**, *19*, 450.
[11] J. J. De Yoreo, N. A. J. M. Sommerdijk, *Nat. Rev. Mater.* **2016**, *1*, 16035.
[12] G. Harding, J. Kosanetzky, U. Neitzel, *Med. Phys.* **1987**, *14*, 515.
[13] Q. Jiang, M. D. Ward, *Chem. Soc. Rev.* **2014**, *43*, 2066.
[14] C. Anduix-Canto, Y.-Y. Kim, Y.-W. Wang, A. Kulak, F. C. Meldrum, H. K. Christenson, *Cryst. Growth Des.* **2016**, *16*, 5403.
[15] B. Cantaert, E. Beniash, F. C. Meldrum, *Chem. - Eur. J.* **2013**, *19*, 14918.
[16] N. Shahidzadeh-Bonn, J. Desarnaud, F. Bertrand, X. Chateau, D. Bonn, *Phys. Rev. E* **2010**, *81*, 066110.
[17] R. M. Espinosa-Marzal, G. W. Scherer, *Acc. Chem. Res.* **2010**, *43*, 897.
[18] E. Doehne, *Geol. Soc. Lon. Spec. Publ.* **2002**, *205*, 51.
[19] A. S. Finnemore, M. R. J. Scherer, R. Langford, S. Mahajan, S. Ludwigs, F. C. Meldrum, U. Steiner, *Adv. Mater.* **2009**, *21*, 3928.
[20] H. Y. Li, H. L. Xin, M. E. Kunitake, E. C. Keene, D. A. Muller, L. A. Estroff, *Adv. Funct. Mater.* **2011**, *21*, 2028.
[21] Y. Levi-Kalisman, G. Falini, L. Addadi, S. Weiner, *J. Struct. Biol.* **2001**, *135*, 8.
[22] M. Prieto, *Mineral. Mag.* **2014**, *78*, 1437.
[23] D. Freyer, W. Voigt, *Monatsh. Chem.* **2003**, *134*, 693.
[24] A. E. S. Van Driessche, T. M. Stawski, M. Kellermeier, *Chem. Geol.* **2019**, *530*, 119274.
[25] J. J. Wray, S. W. Squyres, L. H. Roach, J. L. Bishop, J. F. Mustard, E. Z. N. Dobrea, *Icarus* **2010**, *209*, 416.
[26] T. M. Stawski, R. Besselink, K. Chatzipanagisad, J. Hovelmann, L. G. Benning, A. E. S. Van Driessche, *J. Phys. Chem. C* **2020**, *124*, 8411.
[27] Y.-W. Wang, Y.-Y. Kim, H. K. Christenson, F. C. Meldrum, *Chem. Commun.* **2012**, *48*, 504.
[28] A. Van Driessche, L. Benning, J. Rodriguez-Blanco, M. Ossorio, P. Bots, J. García-Ruiz, *Science* **2012**, *336*, 69.
[29] Y. W. Wang, H. K. Christenson, F. C. Meldrum, *Adv. Funct. Mater.* **2013**, *23*, 5615.
[30] F. Jones, *CrystEngComm* **2012**, *14*, 8374.
[31] T. M. Stawski, A. E. Van Driessche, M. Ossorio, J. D. Rodriguez-Blanco, R. Besselink, L. G. Benning, *Nat. Commun.* **2016**, *7*, 11177.
[32] M. Prieto, C. Viedma, V. Lopezacevedo, J. L. Martinvivaldi, S. Lopezandres, *J. Cryst. Growth* **1988**, *92*, 61.
[33] C. Y. Jia, L. C. Wu, J. L. Fulton, X. R. Liang, J. J. De Yoreo, B. H. Guan, *J. Phys. Chem. C* **2021**, *125*, 3415.
[34] D. Gebauer, P. N. Gunawidjaja, J. Y. P. Ko, Z. Bacsik, B. Aziz, L. J. Liu, Y. F. Hu, L. Bergstrom, C. W. Tai, T. K. Sham, M. Eden, N. Hedin, *Angew. Chem., Int. Ed.* **2010**, *49*, 8889.
[35] M. Ossorio, A. Van Driessche, P. Pérez, J. García-Ruiz, *Chem. Geol.* **2014**, *386*, 16.
[36] J. M. Bell, W. C. Taber, *J. Phys. Chem.* **1906**, *10*, 119.
[37] P. Tian, P. Ning, H. Cao, Z. Li, *J. Chem. Eng. Data* **2012**, *57*, 3664.
[38] T. M. Stawski, H. M. Freeman, A. E. S. Van Driessche, J. Hovelmann, R. Besselink, R. Wirth, L. G. Benning, *Cryst. Growth Des.* **2019**, *19*, 3714.
[39] F. Brandt, D. Bosbach, *J. Cryst. Growth* **2001**, *233*, 837.
[40] A. Torrance, B. W. Darvell, *Aust. Dental J.* **1990**, *35*, 230.
[41] M. Steiger, *J. Cryst. Growth* **2005**, *282*, 455.
[42] M. Steiger, *J. Cryst. Growth* **2005**, *282*, 470.
[43] J. Dewanckele, T. De Kock, M. A. Boone, V. Cnudde, L. Brabant, M. N. Boone, G. Fronteau, L. Van Hoorebeke, P. Jacobs, *Sci. Total Environ.* **2012**, *416*, 436.
[44] J. R. A. Godinho, L. Ma, Y. Chai, M. Storm, T. L. Burnett, *Minerals* **2019**, *9*, 480.
[45] J. Desarnaud, H. Derluyn, L. Molari, S. de Miranda, V. Cnudde, N. Shahidzadeh, *J. Appl. Phys.* **2015**, *118*, 114901.
[46] J. R. Godinho, K. M. Gerke, A. G. Stack, P. D. Lee, *Sci. Rep.* **2016**, *6*, 33086.
[47] J. M. Bray, E. G. Lauchnor, G. D. Redden, R. Gerlach, Y. Fujita, S. L. Codd, J. D. Seymour, *Environ. Sci. Technol.* **2017**, *51*, 1562.
[48] M. Ossorio, T. M. Stawski, J. D. Rodriguez-Blanco, M. Sleutel, J. M. Garcia-Ruiz, L. G. Benning, A. E. S. Van Driessche, *Minerals* **2017**, *7*, 140.
[49] H. K. Christenson, *J. Phys.: Condens. Matter* **2001**, *13*, R95.
[50] Y.-W. Wang, H. K. Christenson, F. C. Meldrum, *Chem. Mater.* **2014**, *26*, 5830.
[51] M. L. Zeng, Y. Y. Kim, C. Anduix-Canto, C. Frontera, D. Laundy, N. Kapur, H. K. Christenson, F. C. Meldrum, *Proc. Natl. Acad. Sci. USA* **2018**, *115*, 7670.
[52] S. Lee, H. S. Wi, W. Jo, Y. C. Cho, H. H. Lee, S. Y. Jeong, Y. I. Kim, G. W. Lee, *Proc. Natl. Acad. Sci. USA* **2016**, *113*, 13618.
[53] D. Selzer, N. Tullmann, A. Kiselev, T. Leisner, M. Kind, *Cryst. Growth Des.* **2018**, *18*, 4896.
[54] P. Laval, A. Crombez, J. B. Salmon, *Langmuir* **2009**, *25*, 1836.
[55] M. A. Levenstein, C. Anduix-Canto, Y. Y. Kim, M. A. Holden, C. G. Nino, D. C. Green, S. E. Foster, A. N. Kulak, L. Govada, N. E. Chayen, S. Day, C. C. Tang, B. Weinhausen, M. Burghammer, N. Kapur, F. C. Meldrum, *Adv. Funct. Mater.* **2019**, *29*, 1808172.
[56] M. A. Holden, T. F. Whale, M. D. Tarn, D. O'Sullivan, R. D. Walshaw, B. J. Murray, F. C. Meldrum, H. K. Christenson, *Sci. Adv.* **2019**, *5*, eaav4316.
[57] J. M. Campbell, F. C. Meldrum, H. K. Christenson, *J. Phys. Chem. C* **2015**, *119*, 1164.
[58] B. H. Guan, L. C. Yang, Z. B. Wu, *Ind. Eng. Chem. Res.* **2010**, *49*, 5569.
[59] S. L. He, J. E. Oddo, M. B. Tomson, *J. Colloid Interface Sci.* **1994**, *163*, 372.
[60] V. Vlachy, *Langmuir* **2001**, *17*, 399.
[61] L. Fumagalli, A. Esfandiar, R. Fabregas, S. Hu, P. Ares, A. Janardanan, Q. Yang, B. Radha, T. Taniguchi, K. Watanabe, G. Gomila, K. S. Novoselov, A. K. Geim, *Science* **2018**, *360*, 1339.
[62] I. C. Bourg, C. I. Steefel, *J. Phys. Chem. C* **2012**, *116*, 11556.
[63] B. H. Guan, G. M. Jiang, Z. B. Wu, J. W. Mao, B. Kong, *J. Am. Ceram. Soc.* **2011**, *94*, 3261.
[64] U. Tritschler, M. Kellermeier, C. Debus, A. Kempter, H. Cölfen, *CrystEngComm* **2015**, *17*, 3772.
[65] U. Tritschler, A. E. Van Driessche, A. Kempter, M. Kellermeier, H. Cölfen, *Angew. Chem., Int. Ed.* **2015**, *54*, 4083.
[66] J. Li, K. S. Liang, G. Scoles, A. Ulman, *Langmuir* **1995**, *11*, 4418.
[67] F. Pfeiffer, *Nat. Photonics* **2018**, *12*, 9.
[68] J. Ihli, M. A. Levenstein, Y. Y. Kim, K. Wakonig, Y. Ning, A. Tatani, A. N. Kulak, D. C. Green, M. Holler, S. P. Armes, F. C. Meldrum, *Chem. Sci.* **2020**, *11*, 355.
[69] P. Bleuet, E. Welcomme, E. Dooryhee, J. Susini, J. L. Hodeau, P. Walter, *Nat. Mater.* **2008**, *7*, 468.
[70] C. Anduix-Canto, M. A. Levenstein, Y. Y. Kim, J. R. A. Godinho, A. N. Kulak, C. Gonzalez, P. J. Withers, J. P. Wright, N. Kapur, H. K. Christenson, F. C. Meldrum; Exploiting Confinement to Study the Crystallization Pathway of Calcium Sulfate; Research Data Leeds Repository; **2021**; https://doi.org/10.5518/1041.